Editors' Suggestion

Piezostrain as a Local Handle to Control Gyrotropic Dynamics of Magnetic Vortices

Vadym Iurchuk,[1,*] Serhii Sorokin,[1] Jürgen Lindner,[1] Jürgen Fassbender,[1,2] and Attila Kákay[1]

[1] *Institute of Ion Beam Physics and Materials Research, Helmholtz-Zentrum Dresden-Rossendorf, 01328 Dresden, Germany*

[2] *Institute of Solid State and Materials Physics, Technische Universität Dresden, 01062 Dresden, Germany*

(Received 17 May 2023; revised 26 July 2023; accepted 9 August 2023; published 31 August 2023)

We present a study of the piezostrain-tunable gyrotropic dynamics in $Co_{40}Fe_{40}B_{20}$ vortex microstructures fabricated on a $0.7Pb[Mg_{1/3}Nb_{2/3}]O_3$-$0.3PbTiO_3$ single-crystal substrate. Using field-modulated-spin-rectification measurements, we demonstrate large frequency tunability (up to 45%) in individual microdisks accessed locally with low surface voltages, and magnetoresistive readout. With increased voltage applied to the substrate, we observe a gradual decrease of the vortex-core gyrotropic frequency associated with the contribution of the strain-induced magnetoelastic energy. The frequency tunability strongly depends on the disk size, with increased frequency downshift for disks with larger diameter. Micromagnetic simulations suggest that the observed size effects originate from the joint action of the strain-induced magnetoelastic and demagnetizing energies in large magnetic disks. These results enable a selective energy-efficient tuning of the vortex gyrotropic frequency in individual vortex-based oscillators with all-electrical operation.

DOI: 10.1103/PhysRevApplied.20.024080

I. INTRODUCTION

Stable topological objects can be spontaneously formed in confined microstructures and nanostructures with high symmetry (e.g., squares, disks, and ellipses) as a result of competition between exchange and magnetostatic energies [1,2]. These topologically protected magnetic states—*magnetic vortices*—are characterized by a curling in-plane magnetization and an out-of-plane singularity in the center of the structure, known as the vortex core (VC) [3]. Resonant excitation of the magnetic vortex by an Oersted field and/or a spin-polarized electrical current results in a dynamical gyrotropic motion of the VC at a specific frequency [4], usually in the subgigahertz range. Resonant VC gyration is successfully used in vortex-based spin-torque oscillators, thanks to the reduced dynamical noise of the VC gyrotropic mode [5–8]. As compared with uniformly magnetized spin-torque oscillators, whose frequencies can be tuned over a wide range due to the nonisochronous property of the auto-oscillation regime, vortex-based oscillators have limited frequency tunability, since the VC gyrotropic frequency is specific to the sample geometry and material parameters. Indeed, the gyration frequency, in the first approximation, is determined by the magnetic properties and the dimensions of the oscillating layer [4]. To overcome this limitation, different approaches have been attempted, including tuning by a bias dc current and/or out-of-plane magnetic field [9], a bias in-plane field and/or rf-current amplitude [10], gyration-frequency modification in magnetostatically coupled vortices [11], or focused-ion-beam-assisted modification of the intrinsic magnetic material parameters [12].

An alternative way uses manipulation of the magnetic vortex configuration by means of static electric fields in composite piezoelectric/ferromagnetic heterostructures via strain-mediated magnetoelectric coupling. This coupling is based on the joint action of two effects: piezoelectric and magnetoelastic (inverse magnetostrictive). Strain-mediated methods of magnetization control recently attracted increased attention due to reduced energy consumption and the possibility of indirect control, avoiding large currents through the magnetic element and/or local-magnetic-field application [13–19]. Regarding magnetic vortices, recent studies demonstrated the possibility to control the vortex configuration [20–23] or even to switch the direction of the vortex circulation or polarization [24,25] in magnetostrictive microdisks grown on piezoelectric substrates on application of an electric field. Theoretical studies show that the vortex gyrotropic mode can also be modified by the introduction of an in-plane magnetoelastic anisotropy, resulting in a decrease of the gyration frequency due to the softening of the restoring-force spring constants [26]. Experimentally, the magnetoelastic-anisotropy-induced

*v.iurchuk@hzdr.de

modification of the vortex gyration frequency was reported in Ref. [27], with use of time-resolved scanning transmission x-ray microscopy of the rf-Oersted-field-driven vortex dynamics in $Co_{40}Fe_{40}B_{20}$ microsquares on mechanically stretched Si_3N_4 membranes. More recently, piezoelectric control over the rf-field-driven vortex gyration trajectories was demonstrated by time-resolved photoemission electron microscopy combined with x-ray-magnetic-circular-dichroism experiments on submicron-sized Ni vortices under strain generated electrically in a piezoelectric $0.7Pb[Mg_{1/3}Nb_{2/3}]O_3$-$0.3PbTiO_3$ (PMN-PT) substrate [28].

One of the major obstacles to using such approaches for spintronic device prototypes is the nonlocal nature of the electrical excitation of the piezosubstrate. Usually, the application of large voltages across the substrate thickness is required, generating bulk strains in an entire piezosubstrate, thus hindering the selective access to and control over individual devices fabricated on a single chip. In addition, a simple electrical detection of the vortex static and/or dynamic behavior, in contrast to cumbersome x-ray-based imaging methods, would facilitate a path towards implementation of strain-tunable spintronic oscillators.

Here we present a study of the piezostrain-tunable vortex-core gyrotropic dynamics in $Co_{40}Fe_{40}B_{20}$ circular microstructures grown on piezoelectric PMN-PT substrates. Using spin-rectification measurements, we demonstrate large gyrotropic frequency tunability (up to 45%) in individual disks accessed locally with low surface voltages (16 V or lower), and all-electrical operation. With increased voltage applied to the PMN-PT substrate, we observe a gradual decrease of the VC gyrotropic frequency associated with the contribution of the strain-induced magnetoelastic energy due to the inverse magnetostrictive (magnetoelastic) effect. Moreover, the frequency tunability strongly depends on the magnetic disk size, with increased frequency downshift for disks with larger diameter. By analyzing the simulated strain-dependent energies for different disk sizes, we attribute the observed size effects to the joint action of the strain-induced magnetoelastic and demagnetizing energies in large magnetic disks.

II. SAMPLE PREPARATION, EXPERIMENTAL SETUP, AND MICROMAGNETIC SIMULATIONS

We use (011)-cut PMN-PT single crystals as functional piezoelectric substrates capable of generating high strains upon application of an electric field [29,30]. Surface electrodes, magnetic microdisks, and the contact pads are fabricated on the PMN-PT substrates in a three-step lithography process. One has to note that for the given PMN-PT compound near the morphotropic phase boundary, the crystallographic rhombohedral-tetragonal phase transition occurs at approximately 90 °C and the ferroelectric Curie temperature is approximately 140 °C [31–33]. Therefore, conventional lithography processes, which include high-temperature prebaking and/or postbaking of the photoresists and electon-beam resists spun on the substrates, may induce irreversible crystallographic phase transitions in PMN-PT. This can potentially degrade its piezoelectric properties due to residual stresses in the crystal or even lead to the formation of cracks on the surface of the crystal, thus making it unsuitable for the microfabrication of thin-film devices. To avoid overheating of the PMN-PT substrate, we developed a specific low-heat three-step fabrication process. First, the surface electrodes to generate a local strain in the PMN-PT substrate are fabricated by UV lithography, electron-beam metallization with Cr(5 nm)/Au(125 nm), and conventional lift-off. As the next step, the magnetostrictive microdisks are patterned by means of electron-beam lithography, followed by magnetron sputtering of a Cr(5 nm)/$Co_{40}Fe_{40}B_{20}$(30 nm)/Cr(2 nm) film and a lift-off. The bottom and top Cr layers are used as seed and cap layers, respectively. The disk diameters are chosen to fulfill the geometric criterion of vortex formation in ferromagnetic disks [34]. As the final step, the contact pads are fabricated by electron-beam lithography, electron-beam evaporation of Cr(5 nm)/Au(50 nm), and lift-off to provide individual electrical access to each microdisk.

To detect the VC dynamics, we use a standard magnetotransport setup with rf capability [see Fig. 1(a)] for electrical detection of magnetization dynamics in single magnetic vortices at room temperature. The detection technique exploits the anisotropic magnetoresistance (MR) effect, i.e., the resistance change induced by the relative angle between the direction of the electric current and the direction of the net magnetization of a magnetic structure. An rf current injected through a bias tee into the microdisk device excites the VC gyrotropic dynamical mode, via the joint action of the spin-transfer torque and the rf Oersted field, and thereby leads to a dynamical magnetoresistance oscillating at the excitation frequency. The time-averaged product of the rf current and the dynamical magnetoresistance—which results in a rectified dc voltage V_{dc}—is measured by a conventional homodyne detection scheme with the use of a lock-in amplifier. When the excitation frequency matches the eigenfrequency of the gyrotropic mode, the resulting V_{dc} is increased due to the dynamical magnetoresistance increase associated with the resonant expansion of the VC gyration trajectory. To increase the signal-to-noise ratio, magnetic field modulation of the dynamical magnetoresistance at the lock-in reference frequency (here 1033 Hz) is used, similarly to what was reported in Refs. [10,35]. To allow electrical excitation of the piezoelectric PMN-PT substrate, a dc voltage $V_P = V_{high} - V_{low}$ is applied between the surface electrodes, as depicted in Fig. 1(a). For all devices, the

distance between the surface electrodes is 10 μm, yielding an electric field of 0.1 MV/m per unit voltage V_P.

For the micromagnetic simulations, we use the graphics-processing-unit-accelerated software package MuMax3 [36] to simulate the magnetization dynamics in the $Co_{40}Fe_{40}B_{20}$ vortices under strain. Similarly to what was reported in Refs. [37,38], the VC dynamics is excited by an in-plane-rf-magnetic-field pulse $b_{rf}\mathrm{sinc}(2\pi f_{cut}t)$ with amplitude $b_{rf} = 2.5$ mT and cutoff frequency $f_{cut} = 2$ GHz. For each simulation, the time evolution of the magnetization is recorded for 200 ns with a time step of 50 ps, and the microwave-absorption power spectra are calculated by performing the Fourier transform of the time-dependent magnetization dynamics. We use the following $Co_{40}Fe_{40}B_{20}$ material parameters: saturation magnetization $M_s = 1100$ kA/m (measured by vibrating-sample magnetometry), exchange constant $A_{ex} = 20$ pJ/m^3, and damping parameter $\alpha = 0.008$. For each disk diameter, we use cells of size $5 \times 5 \times 30$ nm^3 for the magnetization-dynamics simulations, and a finer discretization into $5 \times 5 \times 5$ nm^3 cells for the computation of the equilibrium energies.

III. RESULTS AND DISCUSSION

A. Strain-dependent magnetoresistance

Figure 1(b) shows the typical anisotropic magnetoresistance of a $Co_{40}Fe_{40}B_{20}$ disk with a diameter of 3.65 μm measured for direct current $I_{dc} = 2$ mA and at zero voltage V_P applied to PMN-PT. The top graph in Fig. 1(b) shows the MR curve for the magnetic field $H_\perp$ applied perpendicular to the I_{dc} direction. The bottom graph in Fig. 1(b) shows the MR curve for $H_\parallel$, i.e., for $H \parallel I_{dc}$. The magnetic field is swept from negative to positive saturation. For $H \perp I_{dc}$, when the field is increased from the negative-saturation values ($H_{sat} \approx 40$ mT) towards zero, we observe a resistance growth of approximately 25 mΩ (corresponding to an MR ratio $\eta_\perp = |\Delta R|/R(H_{sat}) \approx 0.015\%$, which is a typical value for Fe-based alloys). This resistance increase indicates a nucleation of a vortex within the $Co_{40}Fe_{40}B_{20}$ disk. Further increase of the magnetic field leads to a VC shift towards the edge of the disk and, eventually, to VC expulsion when the annihilation field H_a is reached. Similarly, for $H \parallel I_{dc}$, the resistance drop of approximately 15 mΩ ($\eta_\parallel \approx 0.015\%$) is measured in the vicinity of $H_\parallel = 0$, in agreement with the angular dependence of the MR.

However, here are two notable observations: first, a large asymmetry of the MR magnitudes for $H \parallel I_{dc}$ and $H \perp I_{dc}$, where $\eta_\perp$ is almost twice as high as $\eta_\parallel$; second, a large difference in the vortex nucleation and annihilation fields is present, depending on the magnetic field orientation. From the magnetoresisance data, we estimate annihilation-field values $\mu_0 H_{a_\perp} = 12$ mT and $\mu_0 H_{a_\parallel} = 8$ mT. This indicates an asymmetric magnetic configuration of the nucleated vortex; otherwise, in the case of a radially symmetric vortex, a rather similar

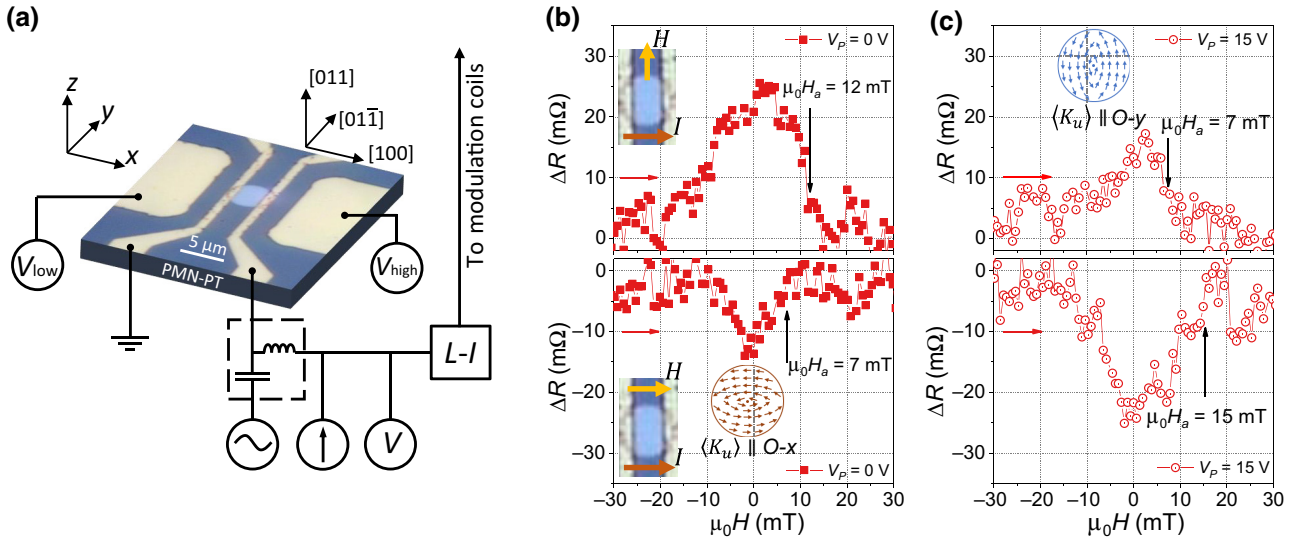

FIG. 1. (a) Schematics of the experiment enabling detection of the magnetization dynamics through rectified-dc-voltage measurements via a lock-in technique, with the simultaneous application of an electric field to the PMN-PT substrate. (b) Magnetoresistance of the $Co_{40}Fe_{40}B_{20}$ disk (diameter $d = 3.65$ μm) measured at $I_{dc} = 2$ mA and $V_P = 0$ V for the magnetic field H applied perpendicular (top graph) and parallel (bottom graph) to the direction of the direct current. The magnetic-field-sweeping direction is indicated by the red arrow. The insets show device images with the corresponding I_{dc} and H directions marked with arrows. (c) Magnetoresistance of the same device as shown in (b) measured at $I_{dc} = 2$ mA and $V_P = 15$ V for $H \perp I_{dc}$ (top graph) and $H \parallel I_{dc}$ (bottom graph). Presumable configurations of the magnetic vortex deduced from the magnetoresistance measurements are schematically depicted in the corresponding insets in (b),(c), with red and blue arrows showing the local direction of the magnetic moments within the disk.

magnetoresistive response would be expected for all in-plane directions of the applied field. The distortion of the vortex configuration is attributed to the presence of the uniaxial magnetic anisotropy, which is typical for sputtered $Co_{40}Fe_{40}B_{20}$ films [39]. In our measurements, $\eta_{\parallel} < \eta_{\perp}$ and $H_{a_{\parallel}} < H_{a_{\perp}}$, which indicates the presence of a nonzero net magnetic anisotropy $\langle K_u \rangle$ along the parallel magnetic field direction, i.e., along the x direction. The corresponding vortex configuration is sketched in the inset in Fig. 1(b). We estimate the anisotropy constant K_{u_x} from the difference between the annihilation fields $H_{a_{\parallel}}$ and $H_{a_{\perp}}$ as $\langle K_{u_x} \rangle = \left(H_{a_{\parallel}} - H_{a_{\perp}}\right)/4M_s$. Using the measured values of $H_{a_{\parallel}}$ and $H_{a_{\perp}}$ and $M_s = 1110$ kA/m (from the magnetometry measurements), we obtain $K_{u_x} \approx 1.1$ kJ/m^3.

Figure 1(c) shows the magnetoresistance curves of the same disk measured for $I_{dc} = 2$ mA under $V_P = 15$ V applied to PMN-PT. We note a drastic qualitative difference between the MR curves measured with $V_P = 15$ V and $V_P = 0$ V. Comparing the MR curves measured for $H \perp I_{dc}$ at $V_P = 0$ V and $V_P = 15$ V [see the top graphs in Figs. 1(b) and 1(c)], we observe two main effects—namely, a reduction of the $\eta_{\perp}$ ratio from 0.015% to 0.01% and a decrease of $H_{a_{\perp}}$ from 12 to 7 mT. On the other hand, for $H \parallel I_{dc}$, an opposite effect is observed, i.e., increase of both $\eta_{\parallel}$ (from 0.008% to 0.015%) and $H_{a_{\parallel}}$ (from 8 to 15 mT).

These voltage-induced effects are explained by the presence of a magnetoelastic anisotropy energy W_{ε} due to the electric-field-induced strain, generated via a converse piezoelectric effect in PMN-PT and transferred to the $Co_{40}Fe_{40}B_{20}$ microdisk. The magnetoelastic energy density is defined as $K_{\varepsilon} = (3/2)\lambda_s Y \langle \varepsilon_{xx} \rangle$, where $\lambda_s = 50$ ppm is the saturation magnetostriction of $Co_{40}Fe_{40}B_{20}$, $Y = 160$ GPa is the Young's modulus of $Co_{40}Fe_{40}B_{20}$, and $\langle \varepsilon_{xx} \rangle$ is the net strain along the x direction, expressed in the dimensionless units of microstrain $\mu\varepsilon = \mu$m/m. We introduce $\langle \varepsilon_{xx} \rangle$ as the effective uniaxial strain generated locally in the small area between the surface electrodes [see Fig. 1(a)]. On the basis of the magnetoresistance measurements and taking into account the positive sign of the $Co_{40}Fe_{40}B_{20}$ magnetostriction constant [40–42], we determine that $\langle \varepsilon_{xx} \rangle < 0$ $\mu\varepsilon$, i.e., the generated strain is compressive along the x direction. Indeed, the observed increase of $\eta_{\parallel}$ and $H_{a_{\parallel}}$ [see the bottom graph in Fig. 1(c)] suggests that, under increasing strain, the net anisotropy $\langle K_{u_x} \rangle$ decreases, in agreement with $\langle \varepsilon_{xx} \rangle < 0$ $\mu\varepsilon$. Under compressive uniaxial strain, the magnetic vortex configuration is distorted, which is manifested as contraction in the direction of the strain and elongation in the direction perpendicular to the strain. Therefore, the compressive strain along the x direction lowers the effective anisotropy in this direction and simultaneously increases the net anisotropy in the perpendicular in-plane direction, i.e., along the O-y direction. This is consistent with the measured reduction of $\eta_{\perp}$ and $H_{a_{\perp}}$ at $V_P = 15$ V, and for the magnetic field perpendicular to the current. The vortex configuration corresponding to the strained state is schematically shown in the inset in Fig. 1(c). One has to note that, in our experiment, the electric field is applied along the [100] crystallographic axis of the PMN-PT crystal and, therefore, compressive strain is expected for a given crystallographic orientation of the PMN-PT crystal [30].

B. Strain-controlled gyration dynamics

Figure 2(a) shows the rectified V_{dc} spectra versus rf-current frequency for a $Co_{40}Fe_{40}B_{20}$ disk with 3.65-μm diameter measured at zero magnetic field and for different values of the voltage V_P applied to the PMN-PT substrate. For all V_P values, the measured resonances have a typical antisymmetric Lorentzian shape, associated with the dominant contribution of the rf Oersted field to the VC gyration dynamics [10,43]. For $V_P = 0$ V, $f_0 = 100$ MHz, in good agreement with the value (112 MHz) analytically predicted by Guslienko's "two-vortices" model [4]. We observe a gradual decrease of the gyrotropic frequency with increasing V_P (i.e., with increasing piezostrain), which is attributed to the magnetoelastic-anisotropy-induced softening of the restoring-force spring constants [26]. For the voltage range used in our experiment ($V_P \leqslant 15$ V), the maximum frequency downshift is 27 MHz (corresponding to 27%) at 15 V, as compared with the initial value at 0 V. Dynamic measurements performed for negative V_P values show a similar frequency shift (see Fig. 5 in the Appendix), since in the quasilinear piezoelectric strain-voltage regime, the generated strain is expected to be equal for both voltage polarities.

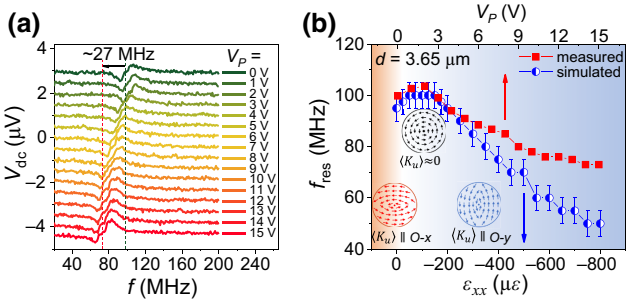

FIG. 2. (a) Frequency-swept zero-field rectification spectra of the 30-nm-thick $Co_{40}Fe_{40}B_{20}$ disk (diameter 3.65 μm) measured at 6 dBm of injected rf power for different voltages V_P applied to PMN-PT. (b) Red squares represent the VC gyrotropic frequency f_0 versus V_P extracted from (a). Blue circles represent simulated values of the gyrotropic frequency versus uniaxial strain ε_{xx}. For the micromagnetic simulations, the uniaxial anisotropy $K_u = 1$ kJ/m^3 $\parallel O$-x is introduced. The sketches show the schematic vortex configurations in the anisotropy-compensation region ($\langle K_u \rangle \parallel O$-$x$), zero-anisotropy region ($\langle K_u \rangle \approx 0$ kJ/m^3), and anisotropy-enhancement region ($\langle K_u \rangle \parallel O$-$y$), respectively (see the main text for details).

For the given V_P range, the displacement current measured between the surface electrodes is below 10 nA, being approximately 6 orders of magnitude smaller than the rms current injected through the disk at 6 dBm. Therefore, we can exclude any voltage-driven heating effects on the observed downshift of the vortex gyrotropic frequency.

Figure 2(b) (red squares) shows the gyrotropic frequency f_0 as a function of V_P. A detailed examination of the $f_0(V_P)$ dependence reveals a nonmonotonous behavior of the gyrotropic frequency—namely, a small increase at low voltages ($V_P \leqslant 2$ V), followed by a steady decrease for $V_P \geqslant 3$ V. To understand this behavior, we conduct micromagnetic simulations of the VC gyration dynamics as a function of the uniaxial strain ε_{xx}. The corresponding $f_0(\varepsilon_{xx})$ dependence is plotted in Fig. 2(b) (blue circles) and is in good agreement with the experimental $f_0(V_P)$ for moderate values of $V_P \leqslant 6$ V, corresponding to uniaxial compressive strain $|\varepsilon_{xx}| \leqslant 350$ $\mu\varepsilon$. Comparison between the experimental $f_0(V_P)$ and the simulated $f_0(\varepsilon_{xx})$ allows for the estimation of the piezoelectrically generated strain per unit electric field E in PMN-PT in the linear regime. We obtain $\varepsilon/E \approx -600$ pm/V, in agreement with typical values of the in-plane piezoelectric constants of PMN-PT. The increased discrepancy between the experimental $f_0(V_P)$ and the simulated $f_0(\varepsilon_{xx})$ at high V_P is related to the nonlinear strain-voltage dependence in the voltage range close to ferroelectric saturation.

In Fig. 2(b) (blue circles), three distinctive regions in the $f_0(\varepsilon_{xx})$ dependence can be differentiated: $|\varepsilon_{xx}| \leqslant 75$ $\mu\varepsilon$, where f_0 increases; 100 $\mu\varepsilon \leqslant |\varepsilon_{xx}| \leqslant 150$ $\mu\varepsilon$, where f_0 is stable; and $|\varepsilon_{xx}| \geqslant 175$ $\mu\varepsilon$, where f_0 decreases. If we take into account the net uniaxial anisotropy $K_{u_x} =$ 1.1 kJ/m^3 in the as-prepared $Co_{40}Fe_{40}B_{20}$ disk (see Sec. III A), these three regions can be associated with the *anisotropy-compensation* region, where $\langle K_u \rangle \parallel O$-$x$; the *zero-anisotropy* region, where $\langle K_u \rangle \approx 0$ kJ/m^3; and the *anisotropy-enhancement* region, where $\langle K_u \rangle \parallel O$-$y$. Indeed, when the compressive strain ε_{xx} increases from 0 $\mu\varepsilon$ to approximately 75 $\mu\varepsilon$, the induced magnetoelastic anisotropy is aligned along the y direction (i.e., perpendicular to the x direction), and competes with the existing net anisotropy along the O-x direction [see the bottom-left sketch in Fig. 2(b)]. The shape of the vortex is, therefore, gradually modified towards the radially symmetric configuration. This manifests itself as an increase of the gyrotropic frequency due to the decrease of the average uniaxial anisotropy. When the strain-induced magnetoelastic anisotropy compensates the intrinsic anisotropy, the net in-plane anisotropy vanishes and the gyrotropic frequency reaches its maximum value, which corresponds to the gyrotropic frequency of the radially symmetric vortex [see the middle sketch in Fig. 2(b)]. Further increase of $|\varepsilon_{xx}|$ leads to enhancement of the net anisotropy along the O-y direction [see the bottom-right sketch in Fig. 2(b)], accompanied by a reduction of the gyrotropic frequency f_0.

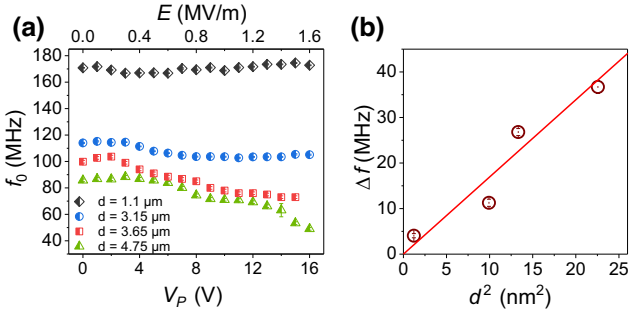

FIG. 3. (a) Gyrotropic frequency versus applied voltage (electric field) for different device diameters d: 1.1 μm (black diamonds); 3.15 μm (blue circles); 3.65 μm (red squares); 4.75 μm (green triangles). (b) Δf versus d^2 extracted from the $f_0(V_P)$ dependencies. The red line is a linear fit to $\Delta f = \text{const} \times d^2$.

Our measurements demonstrate an efficient way to achieve a significant modification of the vortex gyrotropic frequency by piezoelectric strains, generated locally with moderate voltages applied to the piezosubstrate.

C. Size-dependent frequency downshift: Role of the magnetoelastic and demagnetizing energies

Figure 3(a) shows the gyrotropic frequency f_0 versus voltage V_P measured in $Co_{40}Fe_{40}B_{20}$ disks with diameters d of 4.75, 3.65, 3.15, and 1.1 μm. Together with the diameter-dependent gyrotropic frequency f_0, we observe a clear dependence of the maximum frequency downshift Δf on the device size. Here Δf is defined, for each disk diameter, as the difference between the gyrotropic frequency f_0 at $V_P = 0$ V and the minimum attainable f_0 under strain (at $V_P > 0$ V). For $d = 1.1$ μm, the gyrotropic frequency f_0 weakly depends on the voltage V_P, showing a decrease from 171 MHz at zero strain to 166 MHz at $V_P = 5$ V followed by a slight increase back to the original value at higher voltages. The device with $d = 3.15$ μm shows an f_0 drop of 12 MHz (corresponding to a relative decrease of 10.5%) from 114 MHz at $V_P = 0$ V to 102 MHz for $V_P > 9$ V. The devices with larger diameters show a progressively larger strain-induced frequency downshift, i.e., 27 MHz for $d = 3.65$ μm and 36 MHz for $d = 4.75$ μm, corresponding to 27% and 45%, respectively. Figure 3(b) shows Δf versus d^2 for a quasilinear increase of the frequency downshift with increased disk area.

For devices with large diameters (here 4.75 μm), the rectification-signal amplitude decreases for large voltages (strains), and becomes hardly detectable above the noise level for $V_P > 16$ V. This is attributed to the increased ellipticity of the VC trajectory, as a result of the contributions of the strain-induced magnetoelastic and

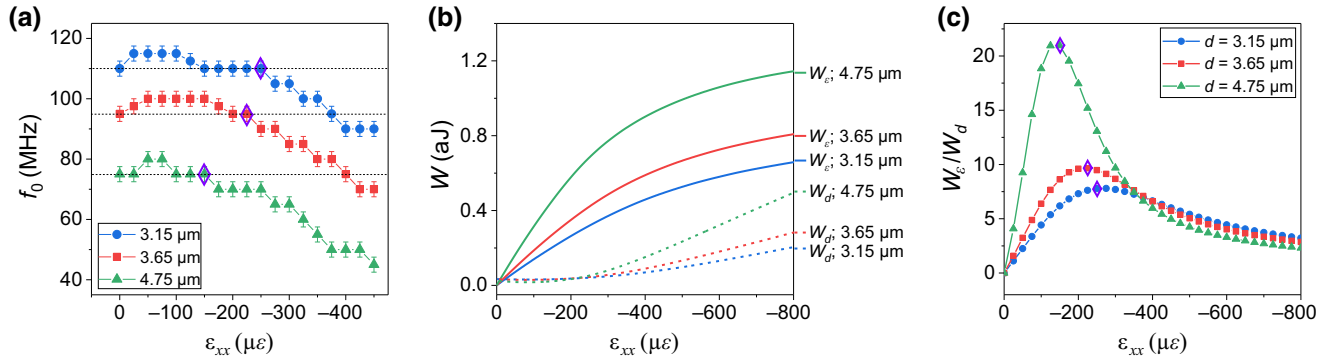

FIG. 4. (a) Simulated $f_0(\varepsilon_{xx})$ for disk diameters of 3.15 μm (blue circles), 3.65 μm (red squares), and 4.75 μm (green triangles). For the given diameter, dotted lines indicate the f_0 level and diamonds mark the onset of the frequency decrease. (b) Calculated values of the magnetoelastic energy W_ε (solid lines) and demagnetizing energy W_d (dashed lines) as a function of strain for $d = 3.15$ μm, 3.65 μm, and 4.75 μm. (c) W_ε/W_d ratio versus ε_{xx} for different values of d. Diamonds mark the onset of the frequency decrease observed in (a).

demagnetizing energies. Therefore, the dynamic magnetoresistance over one gyration period decreases, leading to a reduced rectification signal. In contrast, for the smaller disks, the VC dynamics is equally detectable at higher V_P due to a weaker susceptibility of the VC trajectory to the strain. However, the frequency shift becomes less pronounced, possibly due to strain saturation at large voltages.

To understand the observed size dependence, we calculate the f_0 values as a function of strain for different disk diameters [see Fig. 4(a)]. Here the same magnetic parameters are used as for the simulated data in Fig. 2(b). For increased disk diameter, we observe a reduction of the critical strain, where the onset of the frequency f_0 decrease is observed. This suggests that for larger disks, less magnetoelastic energy is needed to downshift the gyrotropic frequency. Note that this effect does not depend on the magnetic anisotropy, and is present even for $K_u = 0$ kJ/m^3.

To further reveal the origin of the decrease of the critical strain for large disks, we calculate the equilibrium values of the magnetoelastic energy W_ε and the demagnetizing energy W_d as a function of the compressive strain ε_{xx} [see Figs. 4(b) and 4(c)]. We exclude the exchange energy from the consideration due to its negligible value as compared with W_ε and W_d for the given disk sizes. One can see that for small ε_{xx} values, the magnetoelastic energy W_ε dominates [see Fig. 4(b)]; however, the onset of the f_0 decrease, for a given disk diameter, coincides with the onset of the increase of the demagnetizing energy W_d. Figure 4(c) shows the W_ε/W_d ratio versus ε_{xx} for different disk sizes. Here the values of the critical strain (marked with a diamond) correspond to the maximum values of W_ε/W_d, i.e., to the onset of W_d increase. This suggests that besides the magnetoelastic energy contribution, the observed size effects may be related to the increased demagnetizing energy due to the strain-induced distortion of the magnetization distribution in the vortex.

IV. CONCLUSION

We demonstrate a large frequency tunability (up to 45%) in individual $Co_{40}Fe_{40}B_{20}$ disks accessed locally with low surface voltages (16 V or lower) applied to a PMN-PT substrate. Piezostrain-induced tuning and magnetoresistive readout of the VC dynamics via microwave rectification measurements allows an all-electrical operation of the designed microdevices. The observed decrease of the VC gyrotropic frequency is associated with the strain-induced magnetoelastic energy. We show that the frequency tunability strongly depends on the magnetic disk size, with increased frequency shift for the disks with larger diameter. Micromagnetic simulations show that the observed size effects originate jointly from the increased magnetoelastic energy and the increased demagnetizing energy, resulting from the strain-induced distortion of the vortex configuration. Our results show that electrically induced piezostrain offers extra room for the frequency tunability of the VC dynamics in individual spintronic oscillators. In perspective, the frequency tunability for given strain magnitudes can be further enhanced by replacing $Co_{40}Fe_{40}B_{20}$ with large-magnetostriction materials (e.g., Fe_xGa_{1-x}, $TbFe_2$, $DyFe_2$, and Terfenol-D).

ACKNOWLEDGMENTS

This work was funded by the Deutsche Forschungsgemeinschaft through Grant No. IU 5/2-1 (STUNNER)—Project No. 501377640. Support from the Nanofabrication Facilities Rossendorf (NanoFaRo) at the IBC is gratefully acknowledged. We thank Thomas Naumann for help with the growth of $Co_{40}Fe_{40}B_{20}$ thin films. We acknowledge useful discussions with Ciarán Fowley on the details of the low-heat microfabrication process.

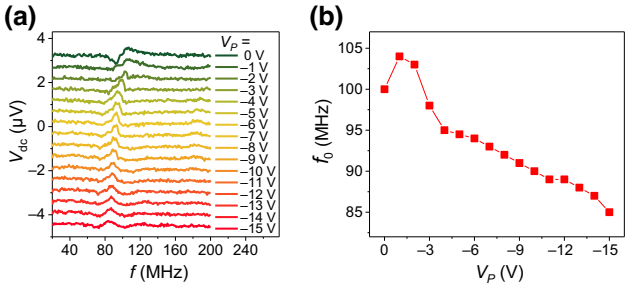

FIG. 5. (a) Frequency-swept zero-field rectification spectra of the 30-nm-thick $Co_{40}Fe_{40}B_{20}$ disk (diameter 3.65 μm) measured at 6 dBm of injected rf power for different negative voltages V_P applied to PMN-PT. (b) VC gyrotropic frequency f_0 versus V_P extracted from the spectra in (a).

We thank Ryszard Narkowicz for help with the implementation of the field modulation in the experimental setup.

APPENDIX: RECTIFICATION SPECTRA FOR NEGATIVE V_P

Figure 5(a) shows the rectified V_{dc} spectra versus rf-current frequency for the $Co_{40}Fe_{40}B_{20}$ disk with 3.65-μm diameter measured at zero magnetic field and for different *negative* values of the voltage V_P applied to the PMN-PT substrate. Figure 5(b) shows the values of the VC gyrotropic frequency f_0 as a function of V_P, extracted from Fig. 5(a).

[1] A. Aharoni, Upper bound to a single-domain behavior of a ferromagnetic cylinder, J. Appl. Phys. **68**, 2892 (1990).

[2] N. A. Usov and S. E. Peschany, Magnetization curling in a fine cylindrical particle, J. Magn. Magn. Mater. **118**, L290 (1993).

[3] T. Shinjo, T. Okuno, R. Hassdorf, K. Shigeto, and T. Ono, Magnetic vortex core observation in circular dots of permalloy, Science **289**, 930 (2000).

[4] K. Y. Guslienko, B. A. Ivanov, V. Novosad, Y. Otani, H. Shima, and K. Fukamichi, Eigenfrequencies of vortex state excitations in magnetic submicron-size disks, J. Appl. Phys. **91**, 8037 (2002).

[5] R. Lebrun, N. Locatelli, S. Tsunegi, J. Grollier, V. Cros, F. Abreu Araujo, H. Kubota, K. Yakushiji, A. Fukushima, and S. Yuasa, Nonlinear Behavior and Mode Coupling in Spin-Transfer Nano-oscillators, Phys. Rev. Appl. **2**, 061001(R) (2014).

[6] R. Lebrun, A. Jenkins, A. Dussaux, N. Locatelli, S. Tsunegi, E. Grimaldi, H. Kubota, P. Bortolotti, K. Yakushiji, J. Grollier, A. Fukushima, S. Yuasa, and V. Cros, Understanding of Phase Noise Squeezing under Fractional Synchronization of a Nonlinear Spin Transfer Vortex Oscillator, Phys. Rev. Lett. **115**, 017201 (2015).

[7] A. Litvinenko, V. Iurchuk, P. Sethi, S. Louis, V. Tyberkevych, J. Li, A. Jenkins, R. Ferreira, B. Dieny, A. Slavin, and U. Ebels, Ultrafast sweep-tuned spectrum analyzer with temporal resolution based on a spin-torque nano-oscillator, Nano Lett. **20**, 6104 (2020).

[8] A. Litvinenko, P. Sethi, C. Murapaka, A. Jenkins, V. Cros, P. Bortolotti, R. Ferreira, B. Dieny, and U. Ebels, Analog and Digital Phase modulation and Signal Transmission with Spin-Torque Nano-oscillators, Phys. Rev. Appl. **16**, 024048 (2021).

[9] A. Dussaux, B. Georges, J. Grollier, V. Cros, A. V. Khvalkovskiy, A. Fukushima, M. Konoto, H. Kubota, K. Yakushiji, S. Yuasa, K. A. Zvezdin, K. Ando, and A. Fert, Large microwave generation from current-driven magnetic vortex oscillators in magnetic tunnel junctions, Nat. Commun. **1**, 1 (2010).

[10] L. Ramasubramanian, V. Iurchuk, S. Sorokin, O. Hellwig, and A. M. Deac, Effects of rf current and bias-field direction on the transition from linear to nonlinear gyrotropic dynamics in magnetic vortex structures, Phys. Rev. B **106**, 214413 (2022).

[11] V. Sluka, A. Kákay, A. M. Deac, D. E. Bürgler, C. M. Schneider, and R. Hertel, Spin-torque-induced dynamics at fine-split frequencies in nano-oscillators with two stacked vortices, Nat. Commun. **6**, 6409 (2015).

[12] L. Ramasubramanian, A. Kákay, C. Fowley, O. Yildirim, P. Matthes, S. Sorokin, A. Titova, D. Hilliard, R. Böttger, R. Hübner, S. Gemming, S. E. Schulz, F. Kronast, D. Makarov, J. Fassbender, and A. Deac, Tunable magnetic vortex dynamics in ion-implanted permalloy disks, ACS Appl. Mater. Interfaces **12**, 27812 (2020).

[13] K. Roy, S. Bandyopadhyay, and J. Atulasimha, Energy dissipation and switching delay in stress-induced switching of multiferroic nanomagnets in the presence of thermal fluctuations, J. Appl. Phys. **112**, 023914 (2012).

[14] K. Roy, Ultra-low-energy non-volatile straintronic computing using single multiferroic composites, Appl. Phys. Lett. **103**, 173110 (2013).

[15] V. Iurchuk, B. Doudin, and B. Kundys, Multistate nonvolatile straintronics controlled by a lateral electric field, J. Phys.: Condens. Matter **26**, 292202 (2014).

[16] V. Iurchuk, B. Doudin, J. Bran, and B. Kundys, Electrical writing of magnetic and resistive multistates in CoFe films deposited onto $Pb[Zr_xTi_{1-x}]O_3$, Phys. Procedia **75**, 956 (2015).

[17] Q. Wang, X. Li, C.-Y. Liang, A. Barra, J. Domann, C. Lynch, A. Sepulveda, and G. Carman, Strain-mediated 180° switching in CoFeB and Terfenol-D nanodots with perpendicular magnetic anisotropy, Appl. Phys. Lett. **110**, 102903 (2017).

[18] J. D. Schneider, Q. Wang, Y. Li, A. C. Chavez, J.-Z. Hu, and G. Carman, RF voltage-controlled magnetization switching in a nano-disk, J. Appl. Phys. **126**, 163903 (2019).

[19] V. Iurchuk, J. Bran, M. Acosta, and B. Kundys, A strain-controlled magnetostrictive pseudo spin valve, Appl. Phys. Lett. **122**, 072404 (2023).

[20] D. E. Parkes, R. Beardsley, S. Bowe, I. Isakov, P. A. Warburton, K. W. Edmonds, R. P. Campion, B. L. Gallagher, A. W. Rushforth, and S. A. Cavill, Voltage controlled modification of flux closure domains in planar magnetic structures for microwave applications, Appl. Phys. Lett. **105**, 062405 (2014).

[21] I. Gilbert, A. C. Chavez, D. T. Pierce, J. Unguris, W.-Y. Sun, C.-Y. Liang, and G. P. Carman, Magnetic microscopy and

simulation of strain-mediated control of magnetization in PMN-PT/Ni nanostructures, Appl. Phys. Lett. **109**, 162404 (2016).

[22] M. Ghidini, R. Pellicelli, R. Mansell, D. Pesquera, B. Nair, X. Moya, S. Farokhipoor, F. Maccherozzi, C. H. W. Barnes, R. P. Cowburn, S. S. Dhesi, and N. D. Mathur, Voltage-driven displacement of magnetic vortex cores, J. Phys. D: Appl. Phys. **53**, 434003 (2020).

[23] M. Ghidini, R. Mansell, R. Pellicelli, D. Pesquera, B. Nair, X. Moya, S. Farokhipoor, F. Maccherozzi, C. H. W. Barnes, R. P. Cowburn, S. S. Dhesi, and N. D. Mathur, Voltage-driven annihilation and creation of magnetic vortices in Ni discs, Nanoscale **12**, 5652 (2020).

[24] Q. Li, A. Tan, A. Scholl, A. T. Young, M. Yang, C. Hwang, A. T. N'Diaye, E. Arenholz, J. Li, and Z. Q. Qiu, Electrical switching of the magnetic vortex circulation in artificial multiferroic structure of Co/Cu/PMN-PT(011), Appl. Phys. Lett. **110**, 262405 (2017).

[25] T. Ostler, R. Cuadrado, R. Chantrell, A. Rushforth, and S. Cavill, Strain Induced Vortex Core Switching in Planar Magnetostrictive Nanostructures, Phys. Rev. Lett. **115**, 067202 (2015).

[26] P. E. Roy, In-plane anisotropy control of the magnetic vortex gyrotropic mode, Appl. Phys. Lett. **102**, 162411 (2013).

[27] S. Finizio, S. Wintz, E. Kirk, A. K. Suszka, S. Gliga, P. Wohlhüter, K. Zeissler, and J. Raabe, Control of the gyration dynamics of magnetic vortices by the magnetoelastic effect, Phys. Rev. B **96**, 054438 (2017).

[28] M. Filianina, L. Baldrati, T. Hajiri, K. Litzius, M. Foerster, L. Aballe, and M. Kläui, Piezo-electrical control of gyration dynamics of magnetic vortices, Appl. Phys. Lett. **115**, 062404 (2019).

[29] S. Zhang, S.-M. Lee, D.-H. Kim, H.-Y. Lee, and T. R. Shrout, Elastic, piezoelectric, and dielectric properties of $0.71Pb(Mg_{1/3}Nb_{2/3})O_3$–$0.29PbTiO_3$ crystals obtained by solid-state crystal growth, J. Am. Ceram. Soc. **91**, 683 (2008).

[30] T. Wu, P. Zhao, M. Bao, A. Bur, J. L. Hockel, K. Wong, K. P. Mohanchandra, C. S. Lynch, and G. P. Carman, Domain engineered switchable strain states in ferroelectric (011) $[Pb(Mg_{1/3}Nb_{2/3})O_3]_{1-x}$-$[PbTiO_3]_x$ (PMN-PT, $x \approx 0.32$) single crystals, J. Appl. Phys. **109**, 124101 (2011).

[31] Y. Guo, H. Luo, K. Chen, H. Xu, X. Zhang, and Z. Yin, Effect of composition and poling field on the properties and ferroelectric phase-stability of $Pb(Mg_{1/3}Nb_{2/3})O_3$–$PbTiO_3$ crystals, J. Appl. Phys. **92**, 6134 (2002).

[32] Y. Guo, H. Luo, D. Ling, H. Xu, T. He, and Z. Yin, The phase transition sequence and the location of the morphotropic phase boundary region in $(1 - x)[Pb(Mg_{1/3}Nb_{2/3})O_3]$–$xPbTiO_3$ single crystal, J. Phys.: Condens. Matter **15**, L77 (2003).

[33] A. S. Makhort, F. Chevrier, D. Kundys, B. Doudin, and B. Kundys, Photovoltaic effect and photopolarization in $[Pb(Mg_{1/3}Nb_{2/3})_{0.68}Ti_{0.32}]O_3$ crystal, Phys. Rev. Materials **2**, 012401(R) (2018).

[34] P.-O. Jubert and R. Allenspach, Analytical approach to the single-domain-to-vortex transition in small magnetic disks, Phys. Rev. B **70**, 144402 (2004).

[35] L. Ramasubramanian, Ph.D. thesis, Technische Universität Chemnitz, 2022.

[36] A. Vansteenkiste, J. Leliaert, M. Dvornik, M. Helsen, F. Garcia-Sanchez, and B. Van Waeyenberge, The design and verification of MuMax3, AIP Adv. **4**, 107133 (2014).

[37] K. Wagner, L. Körber, S. Stienen, J. Lindner, M. Farle, and A. Kákay, Numerical ferromagnetic resonance experiments in nanosized elements, IEEE Magn. Lett. **12**, 1 (2021), conference Name: IEEE Magnetics Letters.

[38] V. Iurchuk, L. Körber, A. M. Deac, J. Faßbender, J. Lindner, and A. Kákay, Stress-induced modification of gyration dynamics in stacked double-vortex structures studied by micromagnetic simulations, J. Phys. D: Appl. Phys. **54**, 475002 (2021).

[39] O. Gladii, R. Salikhov, O. Hellwig, H. Schultheiss, J. Lindner, and R. A. Gallardo, Spin-wave nonreciprocity at the spin-flop transition region in synthetic antiferromagnets, Phys. Rev. B **107**, 104419 (2023).

[40] D. Wang, C. Nordman, Z. Qian, J. M. Daughton, and J. Myers, Magnetostriction effect of amorphous CoFeB thin films and application in spin-dependent tunnel junctions, J. Appl. Phys. **97**, 10C906 (2005).

[41] S. Finizio, S. Wintz, S. Gliga, E. Kirk, A. K. Suszka, P. Wohlhüter, K. Zeissler, and J. Raabe, Unexpected field-induced dynamics in magnetostrictive microstructured elements under isotropic strain, J. Phys.: Condens. Matter **30**, 314001 (2018).

[42] Z. Xiao, R. Lo Conte, M. Goiriena-Goikoetxea, R. V. Chopdekar, C.-H. A. Lambert, X. Li, A. T. N'Diaye, P. Shafer, S. Tiwari, A. Barra, A. Chavez, K. P. Mohanchandra, G. P. Carman, K. L. Wang, S. Salahuddin, E. Arenholz, J. Bokor, and R. N. Candler, Tunable magnetoelastic effects in voltage-controlled exchange-coupled composite multiferroic microstructures, ACS Appl. Mater. Interfaces **12**, 6752 (2020).

[43] J.-S. Kim, M. Kläui, M. V. Fistul, J. Yoon, C.-Y. You, R. Mattheis, C. Ulysse, and G. Faini, Double resonance response in nonlinear magnetic vortex dynamics, Phys. Rev. B **88**, 064402 (2013).